

## Supersensitive Ras activation in dendrites and spines revealed by two-photon fluorescence lifetime imaging

Ryohei Yasuda<sup>1,4</sup>, Christopher D Harvey<sup>1,2</sup>, Haining Zhong<sup>1</sup>, Aleksander Sobczyk<sup>1,3</sup>, Linda van Aelst<sup>2</sup> & Karel Svoboda<sup>1,2</sup>

**To understand the biochemical signals regulated by neural activity, it is necessary to measure protein-protein interactions and enzymatic activity in neuronal microcompartments such as axons, dendrites and their spines. We combined two-photon excitation laser scanning with fluorescence lifetime imaging to measure fluorescence resonance energy transfer at high resolutions in brain slices. We also developed sensitive fluorescent protein-based sensors for the activation of the small GTPase protein Ras with slow (FRas) and fast (FRas-F) kinetics. Using FRas-F, we found in CA1 hippocampal neurons that trains of back-propagating action potentials rapidly and reversibly activated Ras in dendrites and spines. The relationship between firing rate and Ras activation was highly nonlinear (Hill coefficient ~5). This steep dependence was caused by a highly cooperative interaction between calcium ions (Ca<sup>2+</sup>) and Ras activators. The Ras pathway therefore functions as a supersensitive threshold detector for neural activity and Ca<sup>2+</sup> concentration.**

Dendritic spines contain hundreds of signaling molecules associated with the postsynaptic density and actin cytoskeleton<sup>1</sup>. The small GTPase protein Ras signals the calcium concentration ([Ca<sup>2+</sup>]) in neurons to pathways involved in synaptic plasticity<sup>1,2</sup>. Ras activity is controlled by activators (guanine exchange factors, GEFs) and inactivators (GTPase activating proteins, GAPs)<sup>1</sup>. Ras activates the extracellular signal-related kinase (ERK)<sup>1,2</sup>, which is critical for AMPA receptor insertion during long-term potentiation (LTP) in hippocampal neurons<sup>3</sup>, some forms of metabotropic glutamate receptor-dependent long-term depression (LTD)<sup>4</sup> and spine formation<sup>5</sup>. ERK is also important for dendritic protein synthesis and gene transcription, both of which are essential for maintenance of synaptic change<sup>2</sup>.

The Ras-ERK pathway is involved in signaling events that span different compartments, including spines, dendrites and the nucleus. The spatial and temporal dynamics of Ras-ERK signaling are therefore likely to be important in determining the downstream effects. However, most of our knowledge of Ras-ERK signaling and other pathways comes from biochemical experiments that lack spatial resolution.

Understanding the coupling between synaptic activity and signal transduction requires biochemical measurements in dendrites and even individual dendritic spines<sup>1</sup>.

Fluorescence resonance energy transfer (FRET) can be used to image protein-protein interactions in cells. While transferring energy from an excited donor to an acceptor<sup>6</sup>, FRET decreases the donor fluorescence and increases the acceptor fluorescence. Because FRET occurs only when the donor and acceptor are within nanometers of each other, FRET can be used as a readout of numerous protein-protein interactions<sup>6,7</sup>. In addition, sensors can detect Ca<sup>2+</sup> dynamics and the activity of enzymes<sup>7</sup>, including Ras<sup>8,9</sup>.

Although FRET measurements are conceptually simple, quantifying FRET remains challenging<sup>10,11</sup>. Interpreting intensity measurements is complicated because donor and acceptor absorption and emission spectra overlap and fluorescence intensities at any wavelength depend on the expression levels of donor and acceptor. Intensity measurements are further ambiguous because they do not distinguish between a small fraction of interacting molecules with high FRET efficiency ( $Y_{\text{FRET}}$ ) and a large fraction of interacting molecules with low  $Y_{\text{FRET}}$ . To measure FRET in individual dendritic spines in intact tissue, we combined two-photon excitation laser scanning microscopy<sup>12</sup> with fluorescence lifetime imaging (2pFLIM)<sup>13–15</sup>. We developed sensitive Ras sensors based on FRET between fluorescent proteins<sup>8,9</sup>. From 2pFLIM measurements of Ras activation in dendrites and spines, we found that Ras activation is a highly nonlinear function of neural activity and dendritic [Ca<sup>2+</sup>].

## RESULTS

## Measurement of protein binding using 2pFLIM

As a quantitative readout of FRET, we measured the fluorescence lifetime of the donor, defined as the average time between fluorophore excitation and photon emission<sup>6</sup>. After excitation by a short pulse of light from a mode-locked Ti:sapphire laser, the donor excited state typically decays with a single-exponential time course with time constant  $\tau_D$ . Donors bound to acceptors experience FRET, and the usual decay processes collaborate with FRET to dissipate the excited state, thus shortening the fluorescence lifetime to  $\tau_{AD}$ . The FRET

<sup>1</sup>Howard Hughes Medical Institute and <sup>2</sup>Watson School of Biological Science, Cold Spring Harbor Laboratory, Cold Spring Harbor, New York 11724, USA. <sup>3</sup>Department of Physics, State University of New York at Stony Brook, Stony Brook, New York 11794, USA. <sup>4</sup>Present address: Department of Neurobiology, Duke University Medical Center, Durham, North Carolina 27710, USA. Correspondence should be addressed to R.Y. (yasuda@neuro.duke.edu).

Received 22 September 2005; accepted 21 December 2005; published online 22 January 2006; doi:10.1038/nn1635

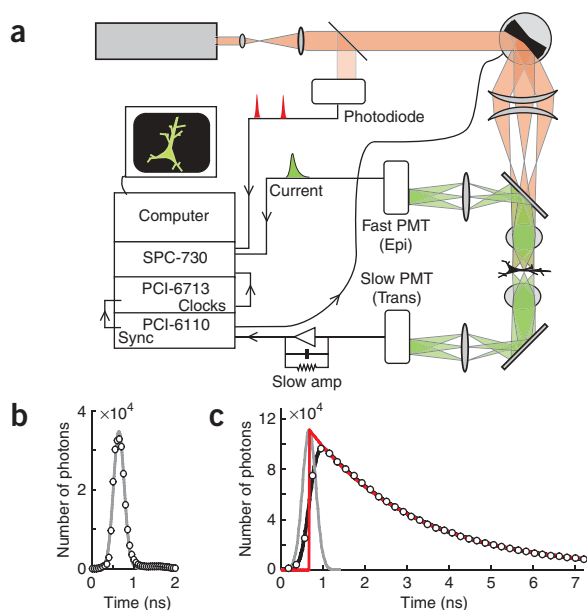


**Figure 1** Two-photon fluorescence lifetime imaging microscopy (2pFLIM) system. **(a)** Wiring of our 2pFLIM system, based on ScanImage<sup>16</sup> ([http://svobodalab.cshl.edu/software\\_main.html](http://svobodalab.cshl.edu/software_main.html)) and a commercial TCSPC imaging board. **(b)** Instrument response function (open circle) and an overlaid Gaussian fit (gray;  $\tau_G = 0.126$  ns). **(c)** Fluorescence lifetime curve of mEGFP. The measured fluorescence curve (open circles) is the convolution of the fluorescence lifetime curve (red;  $\tau_D \sim 2.59$  ns) and the instrument response function (gray; see **b**;  $\tau_G \sim 0.146$  ns). The fluorescence curve (black) was fitted using equation (3).

efficiency can be expressed in terms of measurable quantities as  $Y_{\text{FRET}} = 1 - \tau_{\text{AD}}/\tau_D$ .

In typical experimental situations, free donors coexist with donors bound to acceptors, and the fluorescence decay curve contains two exponentials<sup>6</sup>:

$$F(t) = F_0 \cdot [(1 - P_{\text{AD}}) \exp(-t/\tau_D) + P_{\text{AD}} \exp(-t/\tau_{\text{AD}})] \quad (1)$$

where  $F_0$  is the fluorescence intensity immediately after excitation ( $t = 0$ ). This equation shows that the biologically important ‘binding fraction’ ( $P_{\text{AD}}$ ) can be extracted from the fluorescence decay curve (Methods). Because only the donor fluorescence is involved, fluorescence lifetime measurements of FRET are independent of fluorophore concentrations and are insensitive to spectral bleed-through and wavelength-dependent light scattering.

To image fluorescence lifetimes, we used time-correlated single-photon counting (TCSPC), which measures the time elapsed between laser pulses and fluorescence photons<sup>6</sup>. This technique is ideal for imaging fluorescence lifetime changes during relatively slow ( $> 30$  s) dynamic processes in small compartments<sup>14,15</sup> (Supplementary Note online). We combined a commercial TCSPC board (SPC-730, Becker-Hickl) with our custom-made two-photon microscope<sup>16</sup> (Fig. 1a). By measuring fluorescence lifetimes pixel by pixel, we generated a high-spatial resolution image of fluorescence lifetime. In the TCSPC system, fluorescence decay curves (equation (1)) are convolved with the instrument response, which is defined as the uncertainty in photon arrival times is imposed by our instrumentation (Fig. 1b,c). To calculate  $Y_{\text{FRET}}$  and  $P_{\text{AD}}$ , we took the instrument response into account (Methods). The signal-to-noise ratio was a nonmonotonic function of  $Y_{\text{FRET}}$ . The optimal range for  $Y_{\text{FRET}}$  was  $\sim 0.3$ – $0.7$  (Supplementary Note and Supplementary Fig. 1 online).

### High-sensitivity FRET sensors for Ras activation

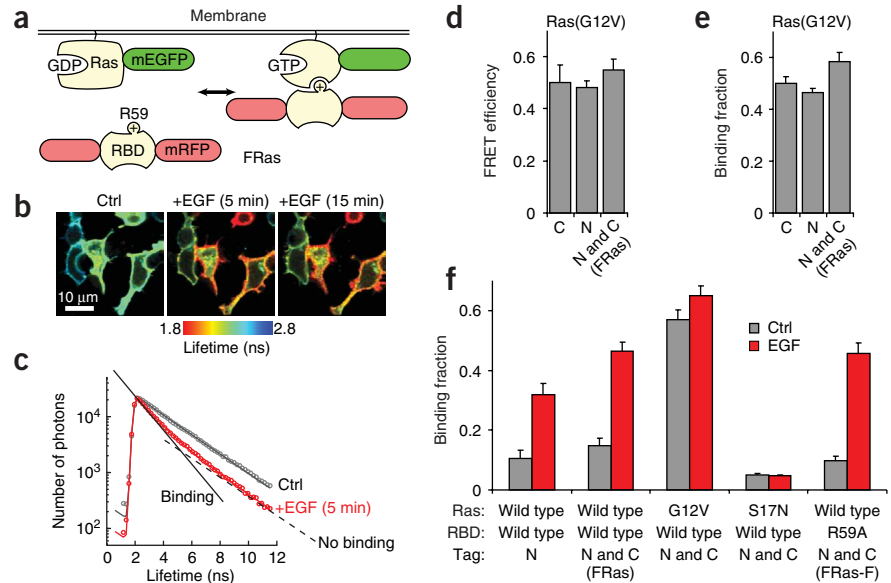
To monitor Ras activation, we developed FRas and FRas-F—FRET sensors for Ras activation<sup>8,9</sup> that are optimized for brightness and FRET efficiency. Enhanced green fluorescent protein (EGFP) and Venus<sup>17</sup> (the brighter variant of enhanced yellow fluorescent protein, EYFP) are bright and have fluorescence lifetime curves that decay with a single exponential, unlike enhanced cyan fluorescent protein (ECFP) or its brighter variant Cerulean<sup>18</sup> (Supplementary Fig. 2 online). In our study, under two-photon excitation, EGFP was brighter than both EYFP and Venus, so we used EGFP as the donor<sup>15,19</sup>. To avoid dimerization of EGFP, we used monomeric EGFP (mEGFP, EGFP A206K)<sup>20</sup>. The red fluorescent proteins mRFP<sup>15</sup> and mCherry were excellent acceptors with negligible spectral bleed-through ( $< 0.5\%$  under our conditions; data not shown).

For any fluorescent protein, populations with and without a functional chromophore coexist in a cell<sup>17</sup>. Because acceptors without a functional chromophore do not contribute to FRET, such acceptors reduce the signal level and lead to an underestimate of the binding fraction. To quantify the fractions of mRFP and mCherry without a functional chromophore, we expressed the fusions mEGFP-mRFP, mRFP-mEGFP and mCherry-mEGFP in HEK293 cells and measured the fluorescence decay curves of mEGFP (Supplementary Fig. 2). The apparent binding fraction (mean  $\pm$  s.e.m.: mEGFP-mRFP =  $0.49 \pm 0.04$ ; mRFP-mEGFP =  $0.57 \pm 0.03$ ; and mCherry-mEGFP =  $0.55 \pm 0.03$ ) suggested that  $\sim 50\%$  of mRFP and mCherry did not function as acceptors. The mEGFP-mRFP (or mEGFP-mCherry) FRET pair thus had a maximum effective binding fraction of  $\sim 0.50$ . Quantitative measurements of binding fraction need to take this factor into account.

### Optimization of FRET sensors for Ras activation

Ras (H-ras) was tagged with mEGFP on its N terminus, and the Ras-binding domain of Raf<sup>21</sup> (RBD) was tagged with mRFP on its C terminus, N terminus or both termini (Fig. 2a). FRas variants were tested in HEK293 cells, which show robust Ras activation in response to epidermal growth factor (EGF) receptor stimulation<sup>22</sup> (Fig. 2b,c). Activation of mEGFP-Ras increased the affinity between RBD-mRFP and mEGFP-Ras, decreasing the fluorescence lifetime of mEGFP-Ras. Because FRET depends on the distance and the angle between donor and acceptor, we optimized the linkers between the fluorescent proteins and Ras/RBD for the signal-to-noise ratio by expressing, in HEK293 cells, a constitutively active Ras mutant (G12V), which has a high affinity for RBD<sup>23</sup>. With our best linkers (Methods), mRFP fusions to either the C or N terminus of RBD showed excellent FRET efficiency (Fig. 2d). The apparent binding fractions under these conditions were  $0.50 \pm 0.02$  for the C terminus and  $0.46 \pm 0.02$  for the N terminus (Fig. 2e). This provided independent confirmation that only one-half of mRFP molecules form functional chromophores (Supplementary Fig. 2). We tested if a pair of acceptors, one at each terminus, would enhance the FRET efficiency. With two ideal acceptors, the fluorescence decay was given by a single exponential with a shorter lifetime than with one acceptor (Supplementary Note). However, the experimental situation was more complex because of incomplete maturation of mRFP and mCherry (Supplementary Fig. 2). We expected that one-fourth of the fusion protein would have two functional acceptors, one-half would have only one functional acceptor, and one-fourth would have two nonfunctional acceptors. In the case of FRas, RBD was fused to mRFP at both the C and the N termini (Fig. 2). The apparent FRET efficiency of this binding population was larger ( $0.55 \pm 0.01$ ) compared to C-terminal only and N-terminal only fusions. The measured binding fraction was also larger with two functional acceptors ( $0.58 \pm 0.04$ ) than with one acceptor (Fig. 2e). Consistent with these results, the change in

**Figure 2** FRET sensors for Ras activation (FRas) in HEK293 Cells. (a) Schematic of FRas. mEGFP was tagged to the N terminus of Ras, and two mRFPs were attached to the N and C termini of RBD. (b) Fluorescence lifetime images in HEK293 cells transfected with FRas, before and after the application of EGF (color coding according to equation (5)). (c) Fluorescence lifetime decay curves corresponding to b. (d–e) The FRET efficiency (d) and binding fraction ( $P_{AD}$ ) (e) between constitutively active Ras mutants (V12G) that were fused with GFP coexpressed with RBD. RBD was tagged with mRFP on (left) the C terminus only, (middle) the N terminus only and (right) the N and C termini. FRET efficiency and binding fractions were calculated from equation (4). (f) Fraction of donor bound to acceptor before and after the application of EGF. Error bars indicate s.e.m. over 4–10 fields from 1–2 dishes. The donor consisted of mEGFP tagged to wild-type Ras, constitutively active Ras (G12V) or constitutively inactive Ras (S17N). The acceptor consisted of mRFP fused to the N terminus of RBD (N), the C terminus of RBD (C) or both (N and C). We used wild-type RBD or RBD mutants with low affinity to Ras (R59A).



the binding fraction in response to EGF was enhanced by tagging RBD with mRFP at both termini, as opposed to tagging it at only the N or only the C terminus (Fig. 2f).

FRas (S17N), the sensor containing the constitutively inactive form of Ras (S17N mutation)<sup>24</sup>, showed a low binding fraction compared to FRas (G12V) (Fig. 2f). Neither S17N nor G12V showed a fluorescence lifetime change after activation of the Ras pathway by EGF (Fig. 2f). These experiments suggest that FRas selectively reports Ras activation in cells.

We further tested FRas in CA1 pyramidal neurons in cultured hippocampal brain slices. A sparse subset of neurons was transfected with FRas using ballistic gene transfer<sup>25</sup>. We measured 2pFLIM on thick apical dendrites, before and after the application of KCl (62.5 mM, 10 min.); these depolarizations open voltage-sensitive calcium channels (VSCCs) and activate Ras<sup>5,26</sup> (Fig. 3a,b). To determine if changes in the FRas fluorescence lifetime reflect the dynamics of endogenous Ras, we did parallel experiments to measure endogenous Ras activation using standard Ras pull-down assays<sup>21</sup> (Fig. 3c,d). Comparing the time course of activation of FRas (Fig. 3b) and endogenous Ras (Fig. 3d) showed that the activation rates were similar; however, after the washout of KCl, the FRas signal decayed much more slowly than did the endogenous Ras activity.

Why is the recovery of FRas slow? Ras inactivators (GAPs) cannot access activated Ras that is bound to RBD<sup>23</sup>. Thus, the overexpression of RBD decreases free concentration of active Ras ([Ras<sup>GTP</sup>]), and thus the rate of Ras<sup>GTP</sup> inactivation, by a factor of

$$\kappa = \frac{[Ras^{GTP}]_{Free}}{[Ras^{GTP}]_{Total}} = \frac{K_D}{[RBD] + K_D} \quad (2)$$

where  $K_D$  is the dissociation constant of RBD and Ras<sup>GTP</sup> (~0.1 μM)<sup>23,27</sup>. Because it is likely that RBD is overexpressed to ~1 μM or more<sup>19</sup>, the GAP activity could be inhibited by more than tenfold compared to the native case. To minimize the effects of the overexpression of RBD on the rate of Ras<sup>GTP</sup> inactivation, we introduced a point mutation (R59A) in RBD, increasing  $K_D$  to several μM (ref. 27). The resulting sensor, FRas-F, reversed rapidly after the removal of KCl (Fig. 3b). In addition, FRas-F showed an improved signal-to-noise ratio compared to FRas in neurons (Fig. 3b) and HEK

293 cells (Fig. 2f), mainly because the baseline binding fraction was decreased. Blocking L-type VSCCs (20-μM nimodipine) partially inhibited Ras activation as reported by both FRas-F and the pull-down assay (Fig. 3b,d). We concluded that FRas-F accurately reports endogenous Ras activation in neurons. FRas-F was used for all subsequent experiments.

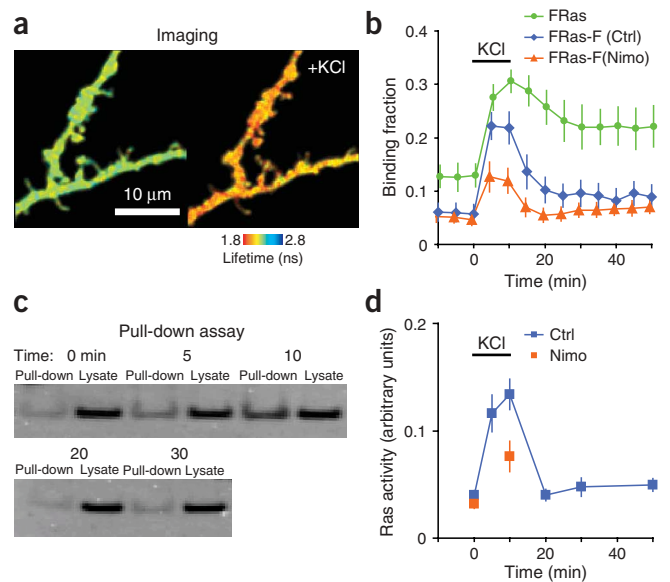


**Figure 3** Ras activation in the apical dendrites of CA1 pyramidal neurons in response to depolarization. (a) Fluorescence lifetime images before and after the application of KCl. (b) Time course of Ras activation measured as the fraction of mEGFP-Ras bound to RBD-mRFP (binding fraction). Nimo, 20 μM nimodipine. Error bars represent s.e.m. over 7–8 cells each. (c) Activity of endogenous Ras. Western blot of active Ras pulled down with GST-RBD beads and total Ras in the lysate. The numbers indicate the time after KCl application (min). KCl was removed at 10 min. (d) Time course of endogenous Ras activity. Error bars represent s.e.m. over 5–8 slices for each time point.

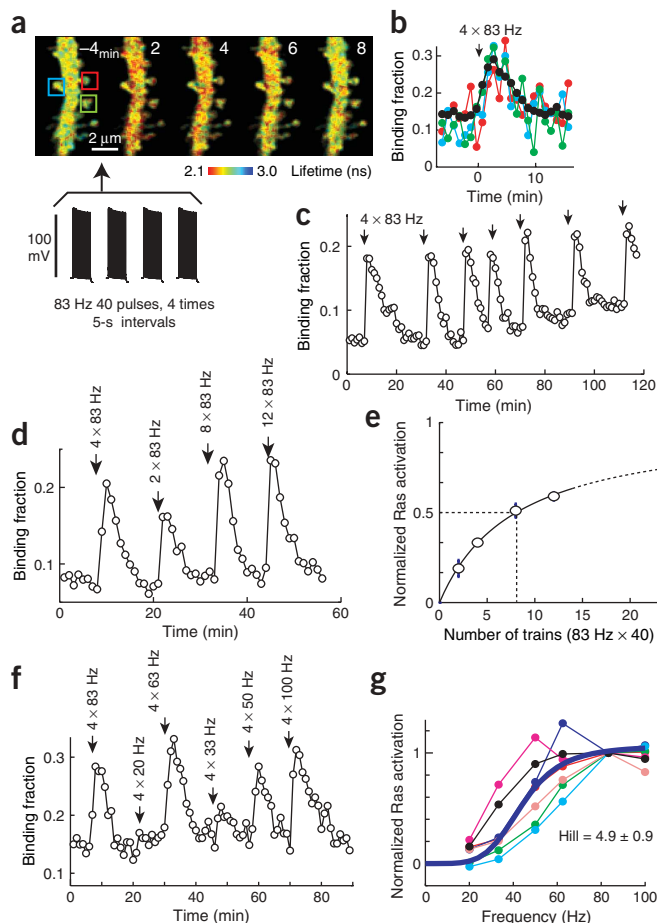


**Figure 4** Action potential-evoked Ras activation in proximal apical dendrites. The stimuli (arrows) consisted of 4 sets of action potential trains, 40 pulses each, repeated at 5-s intervals. **(a)** Fluorescence lifetime image of Ras activation in a dendrite of a cell transfected with FRas-F. **(b)** Time course of Ras activation in spines (colored code as in **a**) and dendrites (black). **(c)** Ras in dendrites can be activated repeatedly with action potential trains (4 sets of action potential trains, 83 Hz, 40 pulses). **(d)** Time course of Ras activation in response to different numbers of action potential trains (83 Hz, 40 pulses). **(e)** Ras activation as a function of number of trains (normalized to Ras activation with four action potential trains). Error bars represent s.e.m.  $n = 5-8$  neurons. The fit is a Michaelis-Menten curve (equation (6)) with Hill coefficient  $H = 1$ . The number of action potential trains for half-saturation was calculated from the fit as  $\sim 8$ . The vertical axis was renormalized to the saturation value obtained from the fit. **(f)** Time course of Ras activation in response to trains of action potentials with different frequencies (number of action potentials was fixed per stimulus). **(g)** Relationship between frequency and Ras activation (normalized to Ras activation at 83 Hz). Thin colored lines are from different cells. Each curve was fit to equation (6); this gave the half-saturation frequency as  $f_{50} = 44 \pm 12$  Hz and the Hill coefficient as  $H = 4.9 \pm 0.9$  ( $n = 7$ ). The thick line shows the best fit with  $f_{50}$  and  $H$  averaged across cells.

We investigated the dependence of Ras activation on the action potential frequency within individual action potential trains. Notably, trains with frequencies below 30 Hz caused little Ras activation, whereas Ras activation seemed to saturate at 50–60 Hz (**Fig. 4f**). Thus Ras activation was a highly nonlinear function of action potential frequency. All recorded neurons showed similar steep saturation behaviors with a large Hill coefficient ( $4.9 \pm 0.9$ ;  $n = 7$ ; fitting to each cell; **Fig. 4g**). The frequency corresponding to 50% saturation ( $f_{50}$ ) was  $44 \pm 12$  Hz. Note that the nonlinearity of the response was not due to FRas-F, because the FRas-F response was linear as a function of the number of action potential trains (**Fig. 4e**, Hill coefficient  $\sim 1$ ). Also, binding between Ras and RBD is known to follow a simple Michaelis-Menten scheme<sup>23,27</sup> (equation (6)). We concluded that the Ras pathway is a supersensitive threshold detector of firing rate in CA1 dendrites.

**Ca<sup>2+</sup>-dependent Ras activation in dendrites and spines**

Ca<sup>2+</sup> couples to Ras activation in neurons. To investigate the relationship between Ras activation and dendritic [Ca<sup>2+</sup>], we measured [Ca<sup>2+</sup>] using low-affinity calcium indicators (167  $\mu$ M Fluo-4FF)<sup>33</sup>. Trains of action potentials produced large [Ca<sup>2+</sup>] transients with a plateau phase (**Fig. 5a**). The amplitude of the plateau [Ca<sup>2+</sup>] was proportional to action potential frequency up to 83 Hz (**Fig. 5b**), consistent with previous measurements<sup>29,31</sup>. The deviation from the straight line at 100 Hz was probably a result of action potential propagation failures<sup>28</sup>. The [Ca<sup>2+</sup>] dynamics were indistinguishable in transfected and untransfected neurons, indicating that transfection with FRas-F affects neither the shape of action potentials nor the densities or properties of VSCCs in the dendritic membrane. Transfection also did not change other cell parameters such as resting potential (transfected:  $-57.1 \pm 1.1$  mV; untransfected:  $-56.7 \pm 0.9$  mV) and input resistance (transfected:  $144 \pm 9$  M $\Omega$ ; untransfected:  $141 \pm 4$  M $\Omega$ ). The linear relationship between action potential frequency and dendritic [Ca<sup>2+</sup>] suggested that the nonlinearity in Ras activation was downstream or independent of Ca<sup>2+</sup>.

Using these data as a ‘ruler’, we derived a relationship between [Ca<sup>2+</sup>] and Ras activation. Ras activation averaged over cells was a highly nonlinear function of [Ca<sup>2+</sup>] (**Fig. 5c**). For the averaged data, the effective Hill coefficient was somewhat lower ( $\sim 3.1$ ) than for individual neurons, mainly because the  $f_{50}$  varied from cell to cell (**Fig. 4g**). A change in [Ca<sup>2+</sup>] (that is,  $\Delta$ [Ca<sup>2+</sup>]) of  $\sim 0.9$   $\mu$ M over  $\sim 1$  s activated Ras to 50%. Therefore, taking into account the resting [Ca<sup>2+</sup>] of the

**Activity-dependent Ras activation in dendrites and spines**

Action potentials propagate into proximal dendrites and spines, opening VSCCs and thus producing relatively global calcium accumulations that last for  $\sim 0.1-1$  s (refs. 28–31). In proximal dendrites (40–80  $\mu$ m from the somata), we measured Ras activation resulting from trains of action potentials (**Fig. 4**). Action potentials were evoked with current injections in the perforated patch-clamp mode<sup>32</sup>, avoiding washout of the Ras sensor and other signaling factors. High-frequency action potential trains (83 Hz  $\times$  40 pulses, 4 times with 5-s intervals) evoked rapid (rise-time  $< 2$  min) and robust Ras activation in dendrites and spines (**Fig. 4a,b**). Ras decayed much more slowly than calcium (decay time constant,  $\tau_{decay} = 4.7 \pm 0.6$  min at 83 Hz;  $4.5 \pm 0.7$  min at 50 Hz;  $3.7 \pm 0.5$  min at 33 Hz;  $n = 7$ ; obtained by dividing the area by the peak amplitude of the transient; **Fig. 4b**). Because of undersampling (1 min per image), we underestimated the peak amplitudes by approximately  $1 - e^{(-0.5 \text{ min} / \tau_{decay})}$ , about 10–13%. We found that Ras activation could be triggered repeatedly, in recordings lasting hours (**Fig. 4c**). In distal dendrites (140–190  $\mu$ m from somata), Ras activation was significantly smaller ( $10 \pm 7\%$  of the signal in proximal dendrites;  $n = 3$ ), presumably due to the attenuation, at high frequencies, of action potential propagation in distal dendrites<sup>28</sup>.

Ras activation increased monotonically with the number of high-frequency trains during a stimulus (**Fig. 4d**) with Michaelis-Menten-type saturation behavior (**Fig. 4e**). Half-saturation was achieved with 8 trains. Therefore, to avoid saturation of the Ras sensor, we set the number of action potential trains per stimulus to four for the rest of the experiments (variable frequency; 40 pulses; 4 times with 5-s intervals).

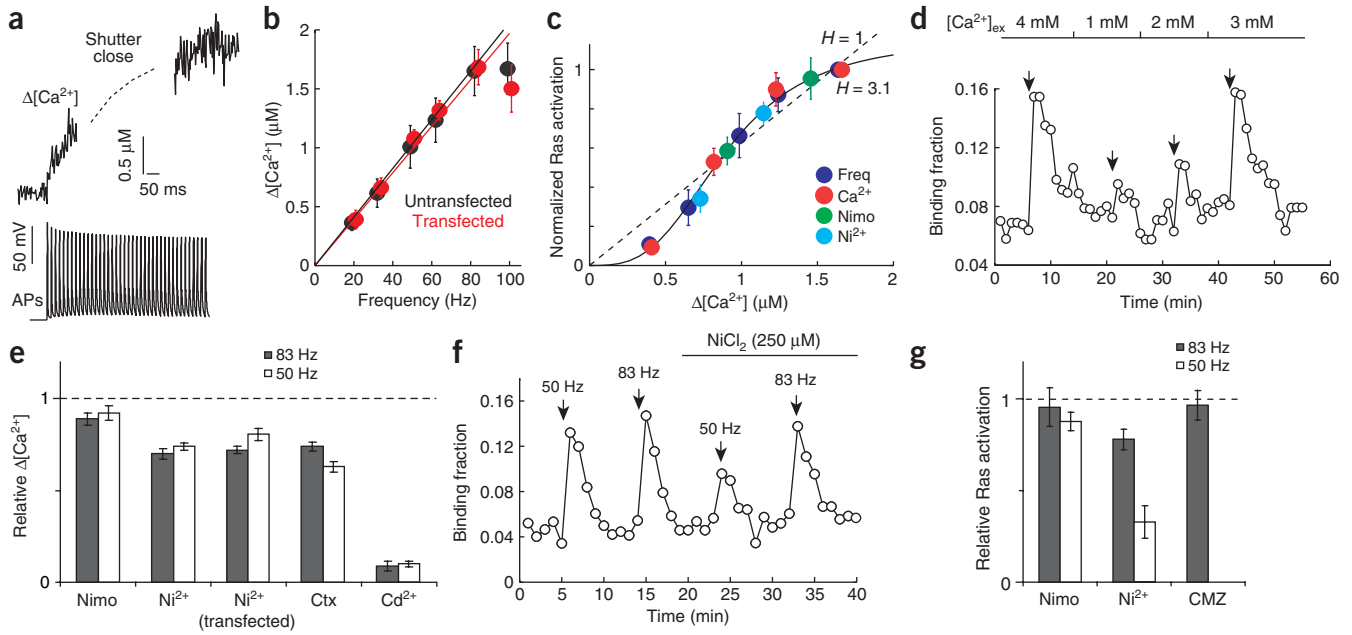


**Figure 5** Coupling between Ras activation and  $[Ca^{2+}]$ . **(a)**  $[Ca^{2+}]$  transient (top) produced by a train of action potentials (bottom), measured using the low-affinity indicator Fluo4-FF. The shutter was closed during the train (dashed line) to reduce photodamage. The amplitude of the  $[Ca^{2+}]$  transient was measured at the end of the action potential train. **(b)** Amplitude of  $[Ca^{2+}]$  transients as a function of action potential frequency. Linear regression lines (transfected, slope  $0.0197 \mu M Hz^{-1}$ ; untransfected,  $0.0206 \mu M Hz^{-1}$ ) are also shown. **(c)** Ras activation (normalized to Ras activation at 83 Hz) as a function of the amplitude of  $[Ca^{2+}]$  transients.  $[Ca^{2+}]$  transients were changed by changing the action potential frequency (blue circles) or extracellular  $[Ca^{2+}]$  (red circles) or by adding nimodipine (Nimo; green circles) or  $Ni^{2+}$  concentration (cyan circles). The fit to the frequency modulation data gave  $\Delta[Ca^{2+}]_{50} = 0.9 \mu M$  and  $H = 3.1$  (equation (6)). Error bars represent s.e.m. ( $n = 7$ ). **(d)** Time course of Ras activation in response to trains of action potentials (APs) in different concentration of extracellular  $[Ca^{2+}]$ . Each stimulus (arrows) consisted of 40 action potentials at 83 Hz, repeated 4 times with 5-s interstimulus intervals. **(e)** Amplitude of  $[Ca^{2+}]$  transients (relative  $\Delta[Ca^{2+}]$ ) in the presence of 20  $\mu M$  nimodipine (Nimo), 250  $\mu M$   $Ni^{2+}$  and a cocktail of 10  $\mu M$   $\omega$ -conotoxin MVIIC and  $\omega$ -conotoxin GVIA (Ctx) or 300  $\mu M$   $Cd^{2+}$ . The conotoxin cocktail was applied by pressure injections into the brain slice through pipettes placed close to patched cells. Each stimulus (arrows) was similar as in **d**, except that the frequency was varied as indicated. Error bars represent s.e.m. (4 neurons each). **(f)** Time course of Ras activation in response to action potential trains before and after the application of  $NiCl_2$  (gray bar). **(g)** Ras activation in the presence of calcium-channel blockers (Nimo or  $Ni^{2+}$ ) or calmodulin blocker (CMZ, 50  $\mu M$ ) relative to control condition. Error bars represent s.e.m. (4 neurons each).

cells<sup>29</sup> ( $\sim 0.1 \mu M$ ), Ras was activated half-maximally by a  $[Ca^{2+}]$  of  $\sim 1 \mu M$  elevated for  $\sim 1$  s.

To test if  $[Ca^{2+}]$  alone determines Ras activation, we manipulated dendritic  $[Ca^{2+}]$  and measured its effect on Ras activation. The  $[Ca^{2+}]$  transient amplitude is proportional to  $[Ca^{2+}]$  in the external solution ( $[Ca^{2+}]_{ex}$ ). While exciting cells with high-frequency action potential trains (83 Hz; **Fig. 4a,b**), we thus varied  $[Ca^{2+}]$  transient amplitudes by changing  $[Ca^{2+}]_{ex}$  (1–4 mM; **Fig. 5d**). The relationship between the amplitude of  $[Ca^{2+}]$  transients and Ras activation was again nonlinear (**Fig. 5c**) and agreed with the relationship obtained from varying the frequency modulation (**Fig. 5c**). These results indicated that  $[Ca^{2+}]$  determined Ras activation.

The Ras-ERK pathway may be activated in  $Ca^{2+}$  microdomains. In particular,  $Ca^{2+}$  entering through L-type channels may preferentially activate the Ras-ERK pathway, even though other channels could dominate  $Ca^{2+}$  accumulations in the cytoplasm<sup>26</sup>. This would suggest that the bulk  $[Ca^{2+}]$  measured in our imaging experiments might not necessarily predict Ras activation. To test this possibility, we blocked subsets of VSCCs and measured dendritic  $[Ca^{2+}]$  and Ras activation in parallel experiments. A nonspecific VSCC blocker (300  $\mu M$   $CdCl_2$ ) reduced  $[Ca^{2+}]$  transient amplitudes by  $>90\%$ , showing that action potential-evoked  $[Ca^{2+}]$  entered the cell almost exclusively through VSCCs (**Fig. 5e**). The use of specific blockers (L-type channel blocker: nimodipine, 20  $\mu M$ ; R-type channel blocker:  $NiCl_2$ , 250  $\mu M$ ; N-type and P/Q-type channel blocker: a cocktail of 10  $\mu M$   $\omega$ -conotoxin

MVIIC and  $\omega$ -conotoxin GVIA; **Fig. 5e**) showed that proximal dendrites of CA1 neurons contain a rich collection of VSCCs:  $\sim 10\%$  L-type,  $\sim 30\%$  R-type, and  $\sim 30\%$  N- and P/Q-type. These results differ from those obtained with  $[Ca^{2+}]$  transients in spines and higher-order dendrites where R-type channels dominate<sup>30</sup>.

Next we measured Ras activation in response to action potential trains in nimodipine or  $NiCl_2$  (**Fig. 5f,g**). Consistent with the small contribution of L-type channels to dendritic  $[Ca^{2+}]$ , nimodipine had little effect at 50 Hz and 83 Hz. In contrast, with  $NiCl_2$ , the extent to which Ras activation was blocked depended on the action potential frequency (**Fig. 5f,g**), as expected from the nonlinear relationship between  $[Ca^{2+}]$  and Ras activation (**Fig. 5c**). As earlier, we obtained the relationship between  $[Ca^{2+}]$  transient amplitudes (from the frequency versus  $[Ca^{2+}]$  relation (**Fig. 5b**) corrected for the fraction blocked after drug applications (**Fig. 5e**)) and Ras activation (normalized to the activation at 83 Hz under the control condition). The results (**Fig. 5c**) were indistinguishable from those obtained by changing action potential frequency or  $[Ca^{2+}]_{ex}$  (**Fig. 5c**). These results suggested that Ras activation is independent of the source of dendritic  $Ca^{2+}$  and that global  $[Ca^{2+}]$  predicts Ras activation.

Cortical neurons contain  $Ca^{2+}$ -dependent modulators of Ras. RasGRF is regulated by calcium-bound calmodulin<sup>34</sup>, and SynGAP is modified by the phosphorylation by calmodulin-dependent kinases, including  $Ca^{2+}$ /calmodulin-dependent protein kinase II (CaMKII)<sup>35,36</sup>. To test if RasGRF or SynGAP shape Ras activation in response to

backpropagating action potentials, we used calmidazolium to block the binding of free calmodulin to its target proteins (Fig. 5g). Calmidazolium blocked the activation of Ras by calcium entering the cytoplasm through NMDA receptors (R.Y., C.D.H. and K.S., unpublished data). Notably, calmidazolium had no effect on Ras activation by action potential trains, suggesting that RasGRF and synGAP were not involved (Fig. 5g).

## DISCUSSION

2pFLIM is a powerful tool to measure protein-protein interactions at the level of single spines in intact tissue. Fluorescence lifetime measurements, which quantify the FRET-dependent quenching of donor fluorescence and enhancement of acceptor fluorescence, have key advantages over standard intensity-based measurements. For example, a simple measure of FRET is the ratio of donor to acceptor fluorescence. Interpretation of this ratio is complicated by spectral bleed-through and by differences in donor and acceptor concentrations. Various methods have been devised to deal with these issues<sup>10</sup>. For example, donor fluorescence can be measured in the presence of the acceptor and after photobleaching of the acceptor<sup>20</sup>, but this procedure is destructive. Another approach involves the use of multiple (three or more) excitation wavelengths<sup>10,11,19</sup>, which is difficult to combine with two-photon microscopy. Intensity measurements can be distorted by wavelength-dependent light scattering. Furthermore, measurements of low signal intensity are sensitive to artifacts. For example, physiological changes in Ras activation of ~10% (Figs. 4 and 5) correspond to fluorescence changes of ~5%. These small signals are easily polluted by movement of the tissue, photobleaching, fluctuations in fluorophore concentration, cellular morphology and light scattering. Additional problems can arise when interactions involve translocation—for example, between the membrane and soluble protein pools. Movement to the membrane can dramatically alter the intensity ratio between donor and acceptor, making bleed-through compensation difficult. Fluorescence lifetime measurements are robust to all these effects. Lifetime measurements allow us to directly calculate the fraction of donor bound to acceptor, even with fairly small numbers of signal photons (Supplementary Note).

Sensors for fluorescence lifetime measurements have different design criteria than those for intensity-based methods. First, it is important that the isolated donor have a single-exponential fluorescence decay so as to allow a straightforward calculation of binding fractions (equation (1)). Second, for fluorescence lifetime measurements, the acceptor quantum efficiency is not important because only the donor fluorescence is used. Acceptors with small quantum efficiencies may even be preferable because this will result in reduced spectral bleed-through. Third, the signal-to-noise ratio is a nonmonotonic function of FRET efficiency (Supplementary Note and Supplementary Fig. 1). Optimization of the signal-to-noise ratio requires sensors with  $Y_{\text{FRET}} \sim 0.5$ . In contrast, for the intensity-based method, the signal-to-noise ratio increases monotonically with  $Y_{\text{FRET}}$ .

The use of fluorescent proteins may impose some limitations. Because only a fraction of acceptors have functional chromophores, the measured binding fraction will be underestimated. We measured the fraction of functional acceptors as ~50% for mRFP and mCherry. For FRas and FRas-F, the maximum apparent binding fraction was ~60% (Fig. 2e,f). Thus, the binding fraction was underestimated by ~40%.

## Ras sensor

Several Ras sensors have been reported. The prototypical sensor Raichu consists of a fusion of ECFP, RBD, Ras (H-Ras without the CAAX tail)

and EYFP, with ECFP anchored in the plasma membrane using the K-Ras CAAX tail<sup>8</sup>. Raichu was not suitable for 2pFLIM measurements in small compartments because of the dim ECFP fluorescence and the small signal generated upon Ras activation. Translocation of RBD tagged with EGFP is also used to measure the activation of untagged Ras<sup>37</sup>. However, this approach is not suitable for small neuronal compartments where the membrane structure cannot be resolved. Similar to FRas, FRET between Ras and RBD tagged with fluorescent proteins is also used<sup>9</sup>. By optimizing the signal and the kinetics of our sensor, we developed a fast, high-sensitivity Ras sensor (FRas-F) optimized for 2pFLIM measurements in small neuronal compartments. By tagging RBD with two mRFPs, we obtained ~20% additional signal (Fig. 2e,f) and thus required ~40% fewer photons to obtain a significant signal-to-noise ratio (Supplementary Note). By reducing the affinity between Ras and RBD, the sensor became reversible with fast decay kinetics (Fig. 3c).

For quantitative measurements of Ras dynamics, the affinity and free concentration of mRFP-RBD-mRFP are important factors. This is analogous to calcium imaging with calcium buffers. High-affinity calcium indicators detect small calcium changes. However, because the indicator reduces free  $[\text{Ca}^{2+}]$ , the extrusion of calcium is inhibited, slowing  $[\text{Ca}^{2+}]$  dynamics. Similarly, the overexpression of high-affinity mRFP-RBD-mRFP slowed the decay of Ras activation by reducing free  $[\text{Ras}^{\text{GTP}}]$  (equation (2)). FRas and FRas-F are thus analogous to high-affinity and low-affinity  $[\text{Ca}^{2+}]$  indicators, respectively<sup>33</sup>. However, unlike the calcium indicator case, the overexpression of high-affinity mRFP-RBD-mRFP did not reduce Ras activation, because the Ras sensor measures the binding ratio of mEGFP-Ras directly.

## Supersensitive Ras response in neurons

$\text{Ca}^{2+}$  accumulation in dendrites and spines can trigger diverse forms of synaptic plasticity<sup>1</sup>. How can one second messenger be involved in diverse, often opposite, outcomes? Supersensitive Ras activation could provide some specificity. Because the Ras signaling pathway shows little activation below a  $[\text{Ca}^{2+}]$  threshold of ~1  $\mu\text{M}$ , minimal cross-talk would exist between Ras signaling and other  $\text{Ca}^{2+}$ -dependent signaling activated at a lower  $[\text{Ca}^{2+}]$ .

Supersensitive signaling can also produce sharp spatial boundaries between active and inactive neuronal domains. Distal dendrites (more than ~150  $\mu\text{m}$  from somata), where most synapses are located, showed little Ras activation with action potential trains, presumably because of decremental action potential back-propagation<sup>28</sup> and the supersensitivity of the Ras pathway.

How is the supersensitivity achieved? In a Goldbeter-Koshland-type switch, the system can become bistable when the activators (GEFs) and deactivators (GAPs) regulating the activity of a protein (Ras) saturate<sup>38</sup>. However, this scheme is not easily reconciled with nonzero basal activity. Another possibility is cooperative calcium binding to calmodulin<sup>31</sup> together with calmodulin-dependent GEFs (RasGRF) or GAPs (synGAP). However, it is unlikely that calmodulin association is the mechanism: blocking the association of calmodulin with calmidazolium did not block Ras activation (Fig. 5g). It is possible that calmodulin is preassociated with a Ras regulator to control its activity. Alternatively, CalDAG-GEFs, a family of GEFs regulated by directly binding  $\text{Ca}^{2+}$  through a pair of EF hands<sup>39</sup>, could contribute to nonlinear Ras activation. Other GAPs, including p120GAP (ref. 40), Ras GTPase activating protein (RASAL)<sup>41</sup> and  $\text{Ca}^{2+}$ -promoted Ras activator (CAPRI)<sup>42</sup>, are translocated to the plasma membrane in a calcium-dependent manner to inactivate Ras. They could suppress Ras responses selectively at low  $[\text{Ca}^{2+}]$  to cause the apparent cooperativity in the relationship between  $[\text{Ca}^{2+}]$  and Ras activation.

In our experiments with trains of backpropagating action potentials, an antagonist of L-type calcium channels (nimodipine) did not block  $[Ca^{2+}]$  transients or Ras activation (Fig. 5e,g). These results are inconsistent with previous reports of selective coupling between L-type channels and ERK activation<sup>5,26,43</sup>. There are several possible explanations for this inconsistency. First, nimodipine may not effectively block L-type channels opened by action potentials, because of their state-dependent blocking kinetics<sup>44</sup>. Second, FRas may not be targeted in the same way as endogenous Ras and may be insensitive to L-type calcium channel microdomains. This is unlikely because L-type channels contributed to similar degrees to the activation of FRas and endogenous Ras when the stimulus was membrane depolarization by KCl application (Fig. 3b,d). Third, most of the studies showing L-type channel–ERK coupling use KCl application, whereas we used backpropagating action potentials. The long depolarizations provided by KCl and postsynaptic potentials favor the opening of L-type channels<sup>45</sup>. Still, our results are inconsistent with a study that showed L-type VSCC–dependent ERK activation by action potential trains<sup>43</sup>. This might be caused by differences in stimulation pattern (theta burst versus regular train) or in the preparation (adult acute slices versus cultured slices from young animals). Fourth, Ras activation might not be sufficient for ERK activation. For example, the opening of L-type channels may be important for blocking the activation of phosphatases that inactivate ERK. Future experiments combining 2pFLIM with electrophysiological assays and  $[Ca^{2+}]$  imaging will help in dissecting the coupling between Ras-ERK activation and  $Ca^{2+}$  sources activated by a variety of physiologically meaningful stimuli. Further experiments are also required to dissect the coupling between L-type channels and the Ras-ERK pathway under physiological conditions.

## METHODS

**Constructs.** mRFP<sup>46</sup>, Cerulean<sup>18</sup>, EGFP-Ras<sup>47</sup>, Venus<sup>17</sup> and EGFP-RBD<sup>48</sup> were gifts from R. Tsien (University of California San Diego), D.W. Piston (Vanderbilt University, Nashville, Tennessee), M. Matsuda (Osaka University, Osaka, Japan), A. Miyawaki (Riken Brain Science Institute, Saitama, Japan) and T. Balla (US National Institutes of Health, Baltimore), respectively. Monomeric EGFP (A206K)<sup>20</sup> and mCherry<sup>49</sup> were generated by mutagenesis from EGFP and mRFP, respectively. mEGFP-Ras and RBD-mRFP were constructed in a pCI expression vector (Promega). FRas consists of mEGFP-Ras (same as that described in ref. 47 except for A206K in EGFP) and mRFP-RBD-mRFP. The linker between RBD and mRFP is YRSTMN for the N terminus and GILQSTVPRARNP for the C terminus. mRFP-RBD-mRFP has a slight tendency to accumulate in the nucleus.

**Preparations.** HEK293 cells were cultured in Dulbecco's modified Eagle's medium (DMEM) and high glucose, supplemented with L-glutamine (Invitrogen) in the presence of 10% fetal bovine serum (FBS). The cells were transfected with mEGFP-Ras and RBD-mRFP using Lipofectamine 2000 (Invitrogen). The molar ratio of mEGFP-Ras and mRFP-RBD-mRFP plasmids was 1:3 or 1:4. After 1–2 d of transfection, cells were serum-starved in 0.2% FBS overnight. Imaging was carried out in a solution containing HEPES buffer (25 mM, pH 7.4), NaCl (114 mM), KCl (2.2 mM),  $CaCl_2$  (2 mM),  $MgCl_2$  (2 mM),  $NaHCO_3$  (22 mM),  $NaH_2PO_4$  (1.1 mM) and glucose (2 mM) at 24–25 °C. To activate Ras, epidermal growth factor (100 ng  $ml^{-1}$ ; EMD Biosciences) was added to the solution.

Hippocampal slices were prepared from postnatal day 6 or 7 rats, as described<sup>50</sup> in accordance with the animal care and use guidelines of Cold Spring Harbor Laboratories. After 1–2 weeks in culture, cells were transfected with ballistic gene transfer<sup>25</sup> (Helios, BioRad). Gold beads (diameter 1.6  $\mu m$ ; 6 mg) were coated with mEGFP-Ras (8  $\mu g$ ) and mRFP-RBD-mRFP (32  $\mu g$ ). Our results showing the slow reversal of FRas (Fig. 3b) suggest that the acceptor (mRFP-RBD-mRFP) concentrations were higher than the donor (mEGFP-RAS) concentrations. To minimize the effects of Ras overexpression on synaptic efficacy<sup>3</sup>, 8 mM  $MgCl_2$  was added (final concentration 10.8 mM) to

the culture medium. After 3–4 d of expression, 2pFLIM imaging was performed in a solution containing NaCl (127 mM), KCl (2.5 mM),  $CaCl_2$  (4 mM),  $MgCl_2$  (4 mM),  $NaHCO_3$  (25 mM),  $NaH_2PO_4$  (1.25 mM) and glucose (25 mM) aerated with 95%  $O_2$  and 5%  $CO_2$  at 24–25 °C. To activate Ras with KCl, the extracellular solution was exchanged to KCl (62.5 mM), NaCl (67 mM),  $CaCl_2$  (4 mM),  $MgCl_2$  (4 mM),  $NaHCO_3$  (25 mM),  $NaH_2PO_4$  (1.25 mM) and glucose (25 mM). To block synaptic receptors, we included 5  $\mu M$  of 2,3-dihydroxy-6-nitro-7-sulfamoyl-benzo(f)quinoxaline (NBQX) and 5  $\mu M$  of R(-)-3-(2-carboxypiperazine-4-yl)-propyl-1-phosphonic acid (D-CPP).

**Instrument response and curve-fitting.** ScanImage<sup>16</sup> uses a data acquisition board (PCI-6110, National Instruments) to control scan mirrors and to acquire fluorescence signals from photomultiplier tubes (PMTs; R3896, Hamamatsu). An additional board (PCI-6713, National Instruments), running on the same clock as the PCI-6110 board, was used to generate frame and line clocks to synchronize the ScanImage and the SPC-730 board. The lifetime decay curve was measured by comparing the times of laser pulses (Ti:sapphire laser, 80 MHz, MaiTai) detected by a photodiode (FDS010, Thorlabs) and photon pulses from a fast PMT. To selectively image mEGFP, we used a bandpass filter (HQ510/70, Chroma) in front of the PMT. The epifluorescence PMT was used for 2pFLIM, and the transfluorescence PMT was used for ScanImage.

In time-domain lifetime measurements, the fluorescence decay curves are convoluted with the pulse response function of the microscope (PRF), also called the instrument response. Assuming a Gaussian PRF (Fig. 1b) and an exponential fluorescence decay curve, the measured function can be expressed as

$$F_{\text{single}}(t) = P \cdot G(t, t_0, \tau_D, \tau_G) \\ = F_0 \frac{1}{2} \exp\left(\frac{\tau_G^2}{2\tau_D} - \frac{t - t_0}{\tau_D}\right) \operatorname{erf}\left(\frac{\tau_G^2 - \tau_D(t - t_0)}{\sqrt{2}\tau_D\tau_G}\right) \quad (3)$$

where  $G$  is the convolution of the Gaussian PRF with standard deviation  $\tau_G$  and an exponential decay with constant  $\tau_D$ , and  $t_0$  is the time offset. The width of the PRF is usually dominated by the transit time spread (TTS) of the photodetector. We used a cooled GaAsP photomultiplier tube (PMT; Hamamatsu H7422-40) with an acceptable TTS ( $\sim 0.3$  ns, full-width at half-maximum (FWHM)) and other favorable properties (for example, quantum efficiency  $\sim 40\%$  and gain  $> 10^6$ ).

To determine the fluorescence decay, one needs to determine the PRF (equation (3)). This can be achieved by directing the pulsed laser directly into the PMT (Fig. 1b). Note that because of the low sensitivity of the PMT in the wavelength regime of the Ti:sapphire laser (700–1000 nm), light that may be strong enough to damage the PMT is required. Therefore, we did not use this method routinely. Instead, we measured a fluorescence decay curve for mEGFP, which decays with a single-exponential time course (Supplementary Fig. 2). We fit the fluorescence decay with equation (3) to obtain the width of the Gaussian ( $\tau_G$ ) as 0.12–0.16 ns (which depends on the applied voltage and so on) and the fluorescence lifetime of mEGFP as  $2.59 \pm 0.01$  ns. Because the noise is proportional to the square root of the number of photons, our fitting routines minimized  $\int dt (\delta F^2)/F$ , where  $\delta F$  is  $F$  subtracted by the theoretical curve.

**Quantifying protein binding in living cells.** One of the key advantages of fluorescence lifetime measurements is that one can quantify the fraction of donor bound to acceptor ( $P_{AD}$ ) independent of  $Y_{FRET}$ . The fluorescence decay needs to be fit with two exponentials with time constants  $\tau_{AD}$  and  $\tau_D$ , corresponding to donor bound to acceptor and free donor. In addition, the PRF (width  $\tau_G$ ) needs to be taken into account:

$$F_{\text{Double}}(t, t_0, \tau_D, \tau_G, \tau_{AD}, P_{AD}) = F_0 \left[ (1 - P_{AD}) \cdot G(t, t_0, \tau_D, \tau_G) + P_{AD} \cdot G(t, t_0, \tau_{AD}, \tau_G) \right] \quad (4)$$

In practice, it is useful to constrain the fit by determining  $\tau_D$ ,  $\tau_G$  and  $\tau_{AD}$  independently under favorable conditions. We measured these parameters in HEK293 cells transfected with FRET sensors. To improve the stability of the fits, we determined  $\tau_D$  and  $\tau_G$  separately without acceptor using equation (3). The remaining parameters—namely,  $t_0$ ,  $F_0$ ,  $P_{AD}$  and  $\tau_{AD}$ —were obtained from measurements with acceptor. The fitting is still unstable when  $P_{AD}$  is small. Therefore, when we measured these parameters for Ras sensors, we used

constitutively active mutants (G12V) to maximize  $P_{AD}$ . The offset arrival time  $t_0$  (0.01 ns) is highly sensitive to the position of the sample (3 mm) and thus should be determined by fitting using the fluorescence decay averaged over all pixels in the image.

**Generation of color coded images.** Because curve fitting is time consuming, it is useful to develop alternative estimates of the fluorescence lifetime to generate color-coded images. The fluorescence lifetime  $\langle \tau \rangle$  averaged over multiple populations is derived from the mean photon arrival time  $\langle t \rangle$  as follows:

$$\langle \tau \rangle = \langle t \rangle - t_0 = \frac{\int dt \cdot tF(t)}{\int dt \cdot F(t)} - t_0 \quad (5)$$

The theoretical value for the average of multiple populations (with decay time constant  $\tau_i$  and fraction  $P_i$  for  $i$ th population) is given by

$$\langle \tau \rangle \sim \frac{\int dt \cdot t \sum_i P_i \cdot \exp(-t/\tau_i)}{\int dt \cdot t \sum_i P_i \cdot \exp(-t/\tau_i)} = \frac{\sum_i P_i \tau_i^2}{\sum_i P_i \tau_i}$$

The mean lifetime was used to generate fluorescence lifetime images (Figs. 2b, 3a and 4a).

**GTP-Ras pull-down assay.** Individual hippocampal slices were incubated at room temperature in artificial cerebrospinal fluid (ACSF) for 30 min followed by stimulation with KCl (62.5 mM) in ACSF containing NBQX (10  $\mu$ M), D-CPP (5  $\mu$ M) and tetrodotoxin (TTX; 1  $\mu$ M). Slices were homogenized by brief sonication in a cold buffer containing HEPES buffer (25 mM; pH 7.5), NaCl (150 mM), 1% Nonidet P-40 (NP-40), 0.25% sodium deoxycholate, 10% glycerol, MgCl<sub>2</sub> (10 mM), EDTA (1 mM), leupeptin (10  $\mu$ g ml<sup>-1</sup>), aprotinin (10  $\mu$ g ml<sup>-1</sup>) and phenylmethylsulphonyl fluoride (PMSF; 0.2 mM). GTP-bound Ras was precipitated from the lysate by incubation at 4 °C for 1 h with purified GST-RBD protein coupled to glutathione-sepharose beads<sup>21</sup>. Aliquots of whole-cell lysate and precipitates of GTP-bound Ras were analyzed by immunoblotting with antibody to Ras (1:1,000; BD Biosciences) and goat anti-mouse secondary antibody conjugated with Alexa Fluor 680 (1:2,000; Molecular Probes). Blots were imaged using the Odyssey Infrared Imaging System (Licor), and fluorescence intensities were obtained using the associated software. Precipitated GTP-bound Ras immunoreactivity was normalized to total Ras immunoreactivity from the whole-cell lysate.

**Electrophysiology.** Perforated patch-clamp recordings were done as described<sup>32</sup> with a patch pipette including potassium gluconate (136.5 mM), KCl (17.5 mM), NaCl (9 mM), MgCl<sub>2</sub> (1 mM), HEPES buffer (10 mM; pH 7.2), EGTA (0.2 mM) and amphotericin B (0.1–0.3 mg ml<sup>-1</sup>). The resulting series resistance was typically 40–200 M $\Omega$ . Action potentials were produced by injecting current (2–6 nA, 4 ms). The relation between Ras activation ( $\Delta$ Ras) and the number of action potential trains ( $N_{AP}$ ), the frequency ( $f$ ) or  $[Ca^{2+}]$  was fitted by Michaelis-Menten curve,

$$\Delta \text{Ras} = \text{Constant} \frac{1}{1 + (X/X_{50})^H} \quad (6)$$

where  $H$  is the Hill coefficient and  $X_{50}$  is  $X$  at which  $\Delta$ Ras is half-saturated.

**Calcium imaging.** Calcium imaging was performed as described<sup>33</sup> using Fluo-4FF (green; 167  $\mu$ M) and Alexa 594 (red; 10  $\mu$ M). The ratio between the change of green fluorescence ( $\Delta G$ ) and red fluorescence ( $R$ ) was used to quantify  $[Ca^{2+}]$  transient ( $\Delta[Ca^{2+}]$ ) as  $\Delta[Ca^{2+}] = \frac{\Delta G/R}{(G/R)_{\text{max}}} K_{D, \text{Fluo4FF}}$ , where  $(G/R)_{\text{max}}$  is the ratio at which calcium saturates when measured in a pipette that includes CaCl<sub>2</sub> (10 mM), and  $K_{D, \text{Fluo4FF}}$  is the dissociation constant of Fluo-4-FF (10  $\mu$ M)<sup>33</sup>.

Note: Supplementary information is available on the Nature Neuroscience website.

**ACKNOWLEDGMENTS**

We thank A. Karpova for mutagenesis of mEGFP; X. Zhang for preparation of cultured slices; R. Tsien (University of California, San Diego), D.W. Piston (Vanderbilt University, Nashville, Tennessee), M. Matsuda (Osaka University, Osaka, Japan), A. Miyawaki (Riken Brain Science Institute, Saitama, Japan) and

T. Balla (US National Institutes of Health) for plasmids; and A. Karpova and V. Iyer for critical reading of the manuscript. The research is supported by the Howard Hughes Medical Institute, the US National Institutes of Health, the New York State Office of Science, Technology and Academic Research, the Burroughs Wellcome Fund (R.Y.), the National Alliance for Research on Schizophrenia and Depression (H.Z.) and a David and Fanny Luke Fellowship (C.D.H.).

**COMPETING INTERESTS STATEMENT**

The authors declare that they have no competing financial interests.

Published online at <http://www.nature.com/natureneuroscience/>  
Reprints and permissions information is available online at <http://ngp.nature.com/reprintsandpermissions/>

- Kennedy, M.B., Beale, H.C., Carlisle, H.J. & Washburn, L.R. Integration of biochemical signalling in spines. *Nat. Rev. Neurosci.* **6**, 423–434 (2005).
- Thomas, G.M. & Huganir, R.L. MAPK cascade signalling and synaptic plasticity. *Nat. Rev. Neurosci.* **5**, 173–183 (2004).
- Zhu, J.J., Qin, Y., Zhao, M., Van Alst, L. & Malinow, R. Ras and Rap control AMPA receptor trafficking during synaptic plasticity. *Cell* **110**, 443–455 (2002).
- Gallagher, S.M., Daly, C.A., Bear, M.F. & Huber, K.M. Extracellular signal-regulated protein kinase activation is required for metabotropic glutamate receptor-dependent long-term depression in hippocampal area CA1. *J. Neurosci.* **24**, 4859–4864 (2004).
- Wu, G.Y., Deisseroth, K. & Tsien, R.W. Spaced stimuli stabilize MAPK pathway activation and its effects on dendritic morphology. *Nat. Neurosci.* **4**, 151–158 (2001).
- Lakowicz, J.R. *Principles of Fluorescence Spectroscopy* 2nd edn. (Plenum, New York, 1999).
- Miyawaki, A. Visualization of the spatial and temporal dynamics of intracellular signalling. *Dev. Cell* **4**, 295–305 (2003).
- Mochizuki, N. *et al.* Spatio-temporal images of growth-factor-induced activation of Ras and Rap1. *Nature* **411**, 1065–1068 (2001).
- Rocks, O. *et al.* An acylation cycle regulates localization and activity of palmitoylated Ras isoforms. *Science* **307**, 1746–1752 (2005).
- Wallrabe, H. & Periasamy, A. Imaging protein molecules using FRET and FLIM microscopy. *Curr. Opin. Biotechnol.* **16**, 19–27 (2005).
- Gordon, G.W., Bery, G., Liang, X.H., Levine, B. & Herman, B. Quantitative fluorescence resonance energy transfer measurements using fluorescence microscopy. *Biophys. J.* **74**, 2702–2713 (1998).
- Denk, W. & Svoboda, K. Photon upmanship: why multiphoton imaging is more than a gimmick. *Neuron* **18**, 351–357 (1997).
- Piston, D.W., Sandison, D.R. & Webb, W.W. Time-resolved fluorescence imaging and background rejection by two-photon excitation in laser-scanning microscopy. in *Time-Resolved Laser Spectroscopy in Biochemistry III* (ed. Lakowicz, J.R.) 379–389 (SPIE, Seattle, 1992).
- Gratton, E., Breusegem, S., Sutin, J., Ruan, Q. & Barry, N. Fluorescence lifetime imaging for the two-photon microscope: time-domain and frequency-domain methods. *J. Biomed. Opt.* **8**, 381–390 (2003).
- Peter, M. *et al.* Multiphoton-FLIM quantification of the EGFP-mRFP1 FRET pair for localization of membrane receptor-kinase interactions. *Biophys. J.* **88**, 1224–1237 (2005).
- Pologruto, T.A., Sabatini, B.L. & Svoboda, K. ScanImage: flexible software for operating laser-scanning microscopes. *Biomed. Eng. Online* **2**, 13 (2003).
- Nagai, T. *et al.* A variant of yellow fluorescent protein with fast and efficient maturation for cell-biological applications. *Nat. Biotechnol.* **20**, 87–90 (2002).
- Rizzo, M.A., Springer, G.H., Granada, B. & Piston, D.W. An improved cyan fluorescent protein variant useful for FRET. *Nat. Biotechnol.* **22**, 445–449 (2004).
- Erickson, M.G., Moon, D.L. & Yue, D.T. DsRed as a potential FRET partner with CFP and GFP. *Biophys. J.* **85**, 599–611 (2003).
- Zacharias, D.A., Violin, J.D., Newton, A.C. & Tsien, R.Y. Partitioning of lipid-modified monomeric GFPs into membrane microdomains of live cells. *Science* **296**, 913–916 (2002).
- de Rooij, J. & Bos, J.L. Minimal Ras-binding domain of Raf1 can be used as an activation-specific probe for Ras. *Oncogene* **14**, 623–625 (1997).
- Medema, R.H., de Vries-Smits, A.M., van der Zon, G.C., Maassen, J.A. & Bos, J.L. Ras activation by insulin and epidermal growth factor through enhanced exchange of guanine nucleotides on p21ras. *Mol. Cell. Biol.* **13**, 155–162 (1993).
- Herrmann, C., Martin, G.A. & Wittinghofer, A. Quantitative analysis of the complex between p21ras and the Ras-binding domain of the human Raf-1 protein kinase. *J. Biol. Chem.* **270**, 2901–2905 (1995).
- Feig, L.A. & Cooper, G.M. Inhibition of NIH 3T3 cell proliferation by a mutant ras protein with preferential affinity for GDP. *Mol. Cell. Biol.* **8**, 3235–3243 (1988).
- McAllister, A.K. Biolistic transfection of neurons. *Sci. STKE* **2000**, pl1 (2000).
- Dolmetsch, R.E., Pajvani, U., Fife, K., Spotts, J.M. & Greenberg, M.E. Signaling to the nucleus by an L-type calcium channel-calmodulin complex through the MAP kinase pathway. *Science* **294**, 333–339 (2001).
- Jaitner, B.K. *et al.* Discrimination of amino acids mediating Ras binding from noninteracting residues affecting raf activation by double mutant analysis. *J. Biol. Chem.* **272**, 29927–29933 (1997).

28. Callaway, J.C. & Ross, W.N. Frequency-dependent propagation of sodium action potentials in dendrites of hippocampal CA1 pyramidal neurons. *J. Neurophysiol.* **74**, 1395–1403 (1995).
29. Maravall, M., Mainen, Z.M., Sabatini, B.L. & Svoboda, K. Estimating intracellular calcium concentrations and buffering without wavelength ratioing. *Biophys. J.* **78**, 2655–2667 (2000).
30. Yasuda, R., Sabatini, B.L. & Svoboda, K. Plasticity of calcium channels in dendritic spines. *Nat. Neurosci.* **6**, 948–955 (2003).
31. Pologruto, T.A., Yasuda, R. & Svoboda, K. Monitoring neural activity and  $[Ca^{2+}]$  with genetically encoded  $Ca^{2+}$  indicators. *J. Neurosci.* **24**, 9572–9579 (2004).
32. Bi, G.Q. & Poo, M.M. Synaptic modifications in cultured hippocampal neurons: dependence on spike timing, synaptic strength, and postsynaptic cell type. *J. Neurosci.* **18**, 10464–10472 (1998).
33. Yasuda, R. *et al.* Imaging calcium concentration dynamics in small neuronal compartments. *Sci. STKE* **2004**, pl5 (2004).
34. Farnsworth, C.L. *et al.* Calcium activation of Ras mediated by neuronal exchange factor Ras-GRF. *Nature* **376**, 524–527 (1995).
35. Chen, H.J., Rojas-Soto, M., Oguni, A. & Kennedy, M.B. A synaptic Ras-GTPase activating protein (p135 SynGAP) inhibited by CaM kinase II. *Neuron* **20**, 895–904 (1998).
36. Kim, J.H., Liao, D., Lau, L.F. & Huganir, R.L. SynGAP: a synaptic RasGAP that associates with the PSD-95/SAP90 protein family. *Neuron* **20**, 683–691 (1998).
37. Chiu, V.K. *et al.* Ras signalling on the endoplasmic reticulum and the Golgi. *Nat. Cell Biol.* **4**, 343–350 (2002).
38. Goldbeter, A. & Koshland, D.E., Jr. An amplified sensitivity arising from covalent modification in biological systems. *Proc. Natl. Acad. Sci. USA* **78**, 6840–6844 (1981).
39. Ebinu, J.O. *et al.* RasGRP, a Ras guanyl nucleotide-releasing protein with calcium- and diacylglycerol-binding motifs. *Science* **280**, 1082–1086 (1998).
40. Davis, A.J., Butt, J.T., Walker, J.H., Moss, S.E. & Gawler, D.J. The  $Ca^{2+}$ -dependent lipid binding domain of P120GAP mediates protein-protein interactions with  $Ca^{2+}$ -dependent membrane-binding proteins. Evidence for a direct interaction between annexin VI and P120GAP. *J. Biol. Chem.* **271**, 24333–24336 (1996).
41. Walker, S.A. *et al.* Identification of a Ras GTPase-activating protein regulated by receptor-mediated  $Ca^{2+}$  oscillations. *EMBO J.* **23**, 1749–1760 (2004).
42. Liu, Q. *et al.* CAPRI and RASAL impose different modes of information processing on Ras due to contrasting temporal filtering of  $Ca^{2+}$ . *J. Cell Biol.* **170**, 183–190 (2005).
43. Dudek, S.M. & Fields, R.D. Somatic action potentials are sufficient for late-phase LTP-related cell signaling. *Proc. Natl. Acad. Sci. USA* **99**, 3962–3967 (2002).
44. Helton, T.D., Xu, W. & Lipscombe, D. Neuronal L-type calcium channels open quickly and are inhibited slowly. *J. Neurosci.* **25**, 10247–10251 (2005).
45. Mermelstein, P.G., Bito, H., Deisseroth, K. & Tsien, R.W. Critical dependence of cAMP response element-binding protein phosphorylation on L-type calcium channels supports a selective response to EPSPs in preference to action potentials. *J. Neurosci.* **20**, 266–273 (2000).
46. Campbell, R.E. *et al.* A monomeric red fluorescent protein. *Proc. Natl. Acad. Sci. USA* **99**, 7877–7882 (2002).
47. Ohba, Y. *et al.* Rap2 as a slowly responding molecular switch in the Rap1 signaling cascade. *Mol. Cell Biol.* **20**, 6074–6083 (2000).
48. Bondeva, T., Balla, A., Varnai, P. & Balla, T. Structural determinants of Ras-Raf interaction analyzed in live cells. *Mol. Biol. Cell* **13**, 2323–2333 (2002).
49. Shaner, N.C. *et al.* Improved monomeric red, orange and yellow fluorescent proteins derived from *Discosoma* sp. red fluorescent protein. *Nat. Biotechnol.* (2004).
50. Stoppini, L., Buchs, P.A. & Muller, D.A. A simple method for organotypic cultures of nervous tissue. *J. Neurosci. Methods* **37**, 173–182 (1991).

## Erratum: Supersensitive Ras activation in dendrites and spines revealed by two-photon fluorescence lifetime imaging

Ryohei Yasuda, Christopher D Harvey, Haining Zhong, Aleksander Sobczyk, Linda van Aelst & Karel Svoboda

*Nature Neuroscience* 9, 283–291 (2006)

In the print version of this article and the version initially published online, the second equation under the heading 'Generation of color coded images' (in Methods) contained an error. The equation should read

$$\langle \tau \rangle \sim \frac{\int dt \cdot t \sum_i P_i \cdot \exp(-t/\tau_i)}{\int dt \cdot \sum_i P_i \cdot \exp(-t/\tau_i)} = \frac{\sum_i P_i \tau_i^2}{\sum_i P_i \tau_i}$$

The error has been corrected in the HTML and PDF versions of the article. This correction has been appended to the PDF version.

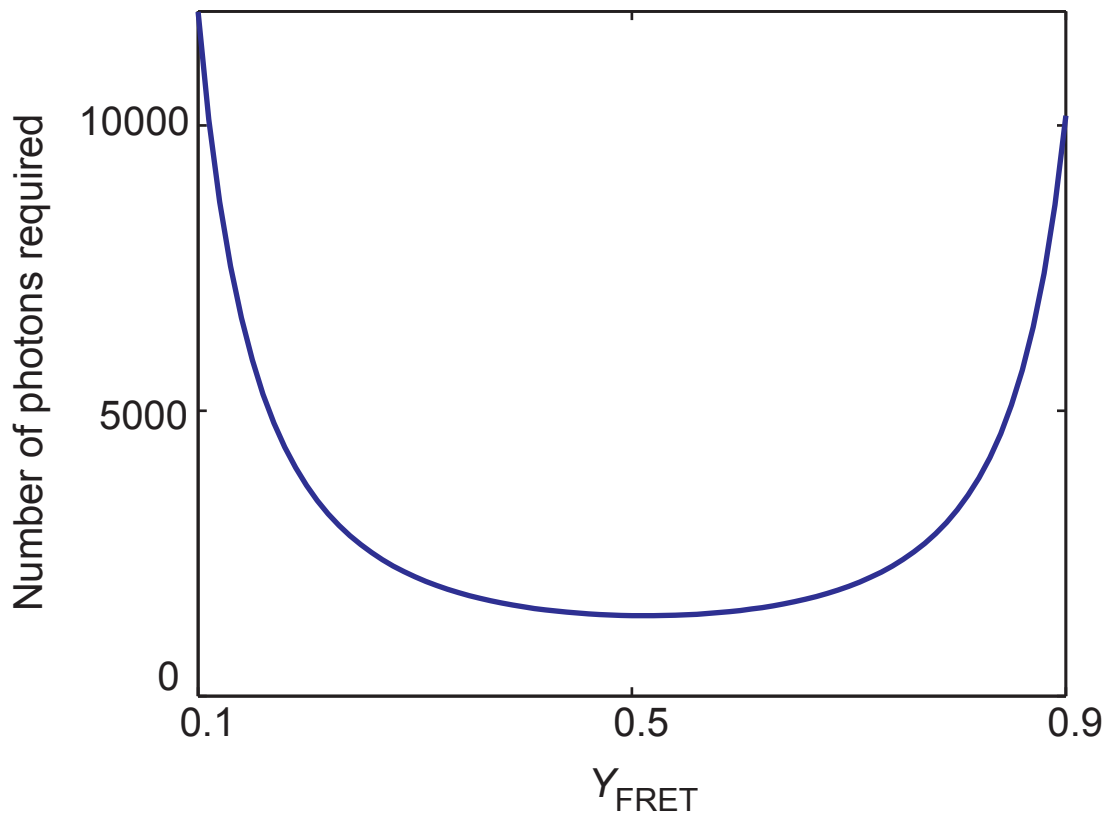
## CORRIGENDUM

## Corrigendum: Activity level controls postsynaptic composition and signaling via the ubiquitin-proteasome system

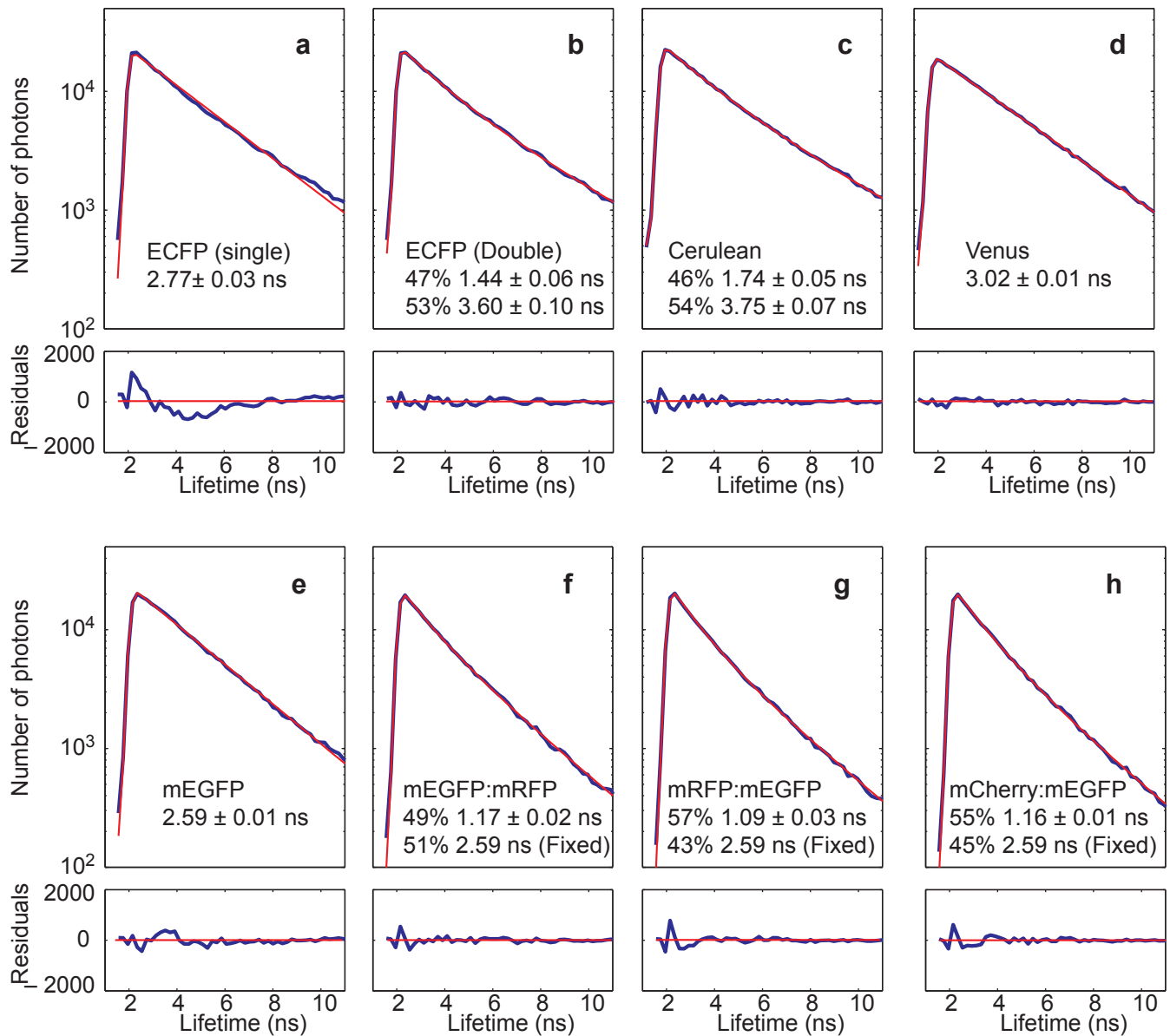
Michael D Ehlers

*Nature Neuroscience* 6, 231–242 (2003)

In the supplementary information initially published online to accompany this article, some values given in Supplementary Tables 1 and 2 were incorrect. The errors have been corrected online. This correction has been appended to the PDF version.



**Supplementary Figure 1.** The number of photons required to detect a change in binding fraction ( $P_{\text{AD}}$ ) from 5 % to 15 % with signal-to-noise ratio  $\sim 1$  as a function of FRET efficiency ( $Y_{\text{FRET}}$ ) (see **Supplementary note 2**).



**Supplementary Figure 2.** Fluorescence decay curves. Fluorescence decay curves (black lines) were fitted (red lines) to single exponentials (Eq. 3, Methods; **a,b** and **e**) or double exponentials (Eq. 4, Methods; **c,d,f, g**). For the fluorescence lifetime decay curves of fusion proteins (**f – h**), curves were fitted to double exponentials (Eq. 4, Methods) while fixing one of the decay constants to the decay time constant for mEGFP (2.59 ns).

## 1. Frequency domain versus time domain measurements of fluorescence lifetime

Methods for fluorescence lifetime measurements fall broadly into two groups: frequency-domain and time-domain<sup>1,2</sup>. Although frequency-domain and time-domain methods are closely related conceptually, they require different instrumentation and have distinct applications. In frequency-domain measurements the excitation light intensity and the detector gain are modulated<sup>3-6</sup> at frequencies in the range of 10MHz - 1GHz. When the excitation intensity is modulated, the fluorescence emission follows the modulation with a smaller amplitude and some phase delay. Measurements of the amplitude and phase provides the fluorescence lifetime,  $\tau_D$ <sup>4,5</sup>. Frequency-domain methods have been used effectively in the context of wide-field fluorescence microscopy employing an image intensifier as a detector<sup>4,7</sup>. In contrast to time-domain measurements, frequency-domain methods allow unlimited signal levels and the potential for better temporal resolution. However, frequency-domain methods are wasteful in terms of signal since only a small fraction (0.1 – 0.25) of detected photons contribute to the signal due to the requirement for detector gain modulation<sup>6</sup>.

Time-domain methods directly measure the fluorescence decay after a brief excitation pulse, typically by measuring the time elapsed between a laser pulse and the arrival of a fluorescence photon (time-correlated single photon counting, TCSPC)<sup>1,8</sup>. For each pixel, a histogram of photon arrival times is computed and stored in computer memory (fluorescence decay). The fluorescence decay is an estimate of the molecular processes encapsulated in **Eq. 1**, convolved with the instrument response, uncertainty of fluorescence lifetime imposed by instrumentation (**Fig. 1b,c**). Estimates of the fluorescence lifetime and interacting population can be derived from these fluorescence decays (Methods).

Since each photon contributes to the signal, time-domain methods have high sensitivity. However, due to limitations in the detection electronics, photon counting rates saturate at fairly low levels ( $\sim 10^6$  photons per second)<sup>1</sup>. For bright samples the excitation levels may have to be kept low to obtain images in a linear signal range. Therefore, time-domain techniques are ideal in situations where fluorescence photons are limiting. On the other hand, sufficient numbers of photons need to be collected to allow curve fitting with adequate signal-to-noise-ratios (SNR) in each pixel. Time-domain methods are therefore relatively slow (*e.g.* 1000 photons per histogram in a  $128 \times 128$  pixels image will require  $\sim 15$  sec of acquisition time). Time-domain methods are easily combined with 2PLSM, since 2PLSM microscopes already use a pulsed laser as a light source<sup>9</sup>. Therefore time-domain methods are ideal for imaging relatively slow ( $> 30$  seconds) dynamic processes in small compartments in scattering tissues.

## 2. The donor fluorescence lifetime with two acceptor chromophores and signal-to-noise ratio in fluorescence lifetime measurements

In the absence of FRET, the fraction of donor in the excited state,  $D^*$ , is governed by

$$\frac{dD^*}{dt} = -k_D D^* + f(t), \quad (\text{Eq. S1})$$

where  $k_D$  is the rate of decay of the excited state (with or without photon emission), and  $f(t)$  is the probability of donor excitation<sup>1</sup>.  $\tau_D = 1 / k_D$  is the mean excited state lifetime. After excitation by

a short pulse of light (pulse duration  $\ll \tau_D$ ), for example from a mode-locked Ti:sapphire laser, the donor excited state typically decays with a single exponential time-course:

$$F = F_0 \cdot \exp(-k_D t) = F_0 \cdot \exp(-t / \tau_D). \quad (\text{Eq. S2})$$

When FRET occurs, the excited state lifetime of the donor is shortened. This is because the usual decay processes are acting together with FRET to dissipate  $D^*$ :

$$\frac{dD^*}{dt} = -k_D D^* - k_{\text{FRET}} D^* + f(t) = -(k_D + k_{\text{FRET}}) D^* + f(t), \quad (\text{Eq. S3})$$

where  $k_{\text{FRET}}$  is the rate of energy transfer<sup>1</sup>. The time-course of the donor fluorescence,  $F$ , follows the time-course of the excited state:

$$F = F_0 \cdot \exp[-(k_D + k_{\text{FRET}})t] = F_0 \cdot \exp(-t / \tau_{\text{AD}}), \quad (\text{Eq. S4})$$

where  $F_0$  is the fluorescence at time 0,  $\tau_{\text{AD}} = 1 / (k_D + k_{\text{FRET}})$  is the fluorescence lifetime of the donor in the presence of the acceptor. The FRET efficiency, which is defined as the fraction of donor fluorescence quenched by acceptor, can be expressed in terms of measurable quantities simply as<sup>1</sup>

$$Y_{\text{FRET}} = 1 - \tau_{\text{AD}} / \tau_D. \quad (\text{Eq. S5})$$

Since only the donor fluorescence is involved, fluorescence lifetime measurements of FRET are independent of fluorophore concentrations and insensitive to wavelength-dependent light scattering.

When binding between donor and acceptor is measured, at least two populations of donor coexist: free donors and donors bound to acceptors. The fluorescence decay curve will then contain two exponentials<sup>1</sup>:

$$F(t) = F_0 \cdot [P_{\text{AD}} \exp(-t / \tau_{\text{AD}}) + P_{\text{D}} \exp(-t / \tau_D)], \quad (\text{Eq. S6})$$

where  $P_{\text{AD}}$  and  $P_{\text{D}}$  are the fraction of donor bound and unbound to acceptor, respectively ( $P_{\text{AD}} + P_{\text{D}} = 1$ ). From a biological perspective deriving  $P_{\text{AD}}$  is of considerable interest, as this corresponds to binding fraction.

With two acceptors, the fluorescence decay of the excited state of donor ( $D^*$ ) is given by

$$\frac{dD^*}{dt} = -(k_D + k_{1,\text{FRET}} + k_{2,\text{FRET}}) D^* + f(t), \quad (\text{Eq. S7})$$

where  $k_{1,\text{FRET}}$  and  $k_{2,\text{FRET}}$  are the rates of energy transfer to each acceptor. Thus, the fluorescence decay is given by a single exponential with a shorter lifetime than with one acceptor. The total FRET efficiency can be expressed in terms of the FRET efficiencies for each acceptor ( $Y_{1,\text{FRET}}$  and  $Y_{2,\text{FRET}}$ ) as

$$Y_{\text{FRET}} = 1 - \left[ 1 + \frac{Y_{1,\text{FRET}}}{1 - Y_{1,\text{FRET}}} + \frac{Y_{2,\text{FRET}}}{1 - Y_{2,\text{FRET}}} \right]^{-1}. \quad (\text{Eq. S8})$$

In fluorescence lifetime measurements, the signal-to-noise-ratio (SNR) is dominated by shot noise. The error in estimating the mean fluorescence lifetime  $\langle \tau \rangle$ ,  $\delta \langle \tau \rangle$ , is given by

$$\frac{\delta \langle \tau \rangle}{\langle \tau \rangle} = n^{-1/2}, \quad (\text{Eq. S9})$$

where  $n$  is the number of photons contributing to the measurement<sup>6</sup>. From **Eq. S6**, the theoretical values of  $\langle \tau \rangle$  are given by

$$\langle \tau \rangle = \frac{\int dt t [P_{\text{D}} \cdot \exp(-t/\tau_{\text{D}}) + P_{\text{AD}} \cdot \exp(-t/\tau_{\text{AD}})]}{\int dt [P_{\text{D}} \cdot \exp(-t/\tau_{\text{D}}) + P_{\text{AD}} \cdot \exp(-t/\tau_{\text{AD}})]} = \frac{P_{\text{D}}\tau_{\text{D}}^2 + P_{\text{AD}}\tau_{\text{AD}}^2}{P_{\text{D}}\tau_{\text{D}} + P_{\text{AD}}\tau_{\text{AD}}}. \quad (\text{Eq. S10})$$

Thus the binding fraction  $P_{\text{AD}}$  can be obtained from  $\langle \tau \rangle$  as

$$P_{\text{AD}} = \frac{\tau_{\text{D}}(\tau_{\text{D}} - \langle \tau \rangle)}{(\tau_{\text{D}} - \tau_{\text{AD}})(\tau_{\text{D}} + \tau_{\text{AD}} - \langle \tau \rangle)}. \quad (\text{Eq. S11})$$

Thus the error in the measurement of  $P_{\text{AD}}$ ,  $|\delta P_{\text{AD}}|$ , can be obtained by differentiation of **Eq. S11** as

$$|\delta P_{\text{AD}}| = A \frac{\delta \langle \tau \rangle}{\langle \tau \rangle} = A n^{-1/2}, \quad (\text{Eq. S12})$$

where  $A$  is

$$A = \frac{P_{\text{D}}^2 + P_{\text{AD}}^2(1 - Y_{\text{FRET}})^3 + P_{\text{D}}P_{\text{AD}}(1 - Y_{\text{FRET}})(2 - Y_{\text{FRET}})}{Y_{\text{FRET}}(1 - Y_{\text{FRET}})}. \quad (\text{Eq. S13})$$

Thus, the number of photons required to detect a change in  $P_{\text{AD}}$  ( $\Delta P_{\text{AD}}$ ) with SNR  $\sim 1$  is given by

$$n_{\text{SNR}=1} = \left( \frac{((1 - P_{\text{AD}})^2 + P_{\text{AD}}^2(1 - Y_{\text{FRET}})^3 + (1 - P_{\text{AD}})P_{\text{AD}}(1 - Y_{\text{FRET}})(2 - Y_{\text{FRET}}))}{\Delta P_{\text{AD}} Y_{\text{FRET}} (1 - Y_{\text{FRET}})} \right)^2. \quad (\text{Eq. S14})$$

For example, for our Ras sensor FRas  $Y_{\text{FRET}} = 0.55$ , and under typical conditions  $P_{\text{AD}} \sim 0.05$ . Thus, to detect a 10 % binding change,  $\sim 1500$  photons are required. **Eq. S14** shows that the required number of photons decreases as  $\sim Y_{\text{FRET}}^{-2}$  for moderate FRET efficiencies ( $Y_{\text{FRET}} < 0.3$ ) (**Supplementary Figure 1**). It is therefore critical to use or develop sensors with high FRET

efficiency. Surprisingly, the SNR is a non-monotonic function of  $Y_{\text{FRET}}$ . At large  $Y_{\text{FRET}}$  ( $> 0.5$ ) the required number of photons for a given signal to noise ratio increases, because the short lifetime component is difficult to detect against the background of the long lifetime component. The optimal range is  $Y_{\text{FRET}} \sim 0.3 - 0.7$ .

## References

1. Lakowicz, J. R. Principles of Fluorescence Spectroscopy (Plenum, NY, USA, 1999).
2. Gratton, E., Breusegem, S., Sutin, J., Ruan, Q. & Barry, N. Fluorescence lifetime imaging for the two-photon microscope: time-domain and frequency-domain methods. *J. Biomed. Opt.* 8, 381–390 (2003).
3. Piston, D. W., Sandison, D. R. & Webb, W. W. in Time-Resolved Laser Spectroscopy in Biochemistry III (ed. Lakowicz, J. R.) 379-389 (SPIE, Seattle, 1992).
4. Squire, A., Verveer, P. J. & Bastiaens, P. I. Multiple frequency fluorescence lifetime imaging microscopy. *J. Microsc.* 197 ( Pt 2), 136-49 (2000).
5. So, P. T. C. et al. Time-resolved fluorescence microscopy using two-photon excitation. *Bioimaging* 3, 49-63 (1995).
6. Philip, J. & Carlsson, K. Theoretical investigation of the signal-to-noise ratio in fluorescence lifetime imaging. *J. Opt. Soc. Am. A* 20, 368-379 (2003).
7. Verveer, P. J., Wouters, F. S., Reynolds, A. R. & Bastiaens, P. I. Quantitative imaging of lateral ErbB1 receptor signal propagation in the plasma membrane. *Science* 290, 1567-70. (2000).
8. Becker, W., Bergmann, K., Koenig, K. & Tirlapur, U. Picosecond fluorescence lifetime microscopy by TCSPC imaging. *Proc. SPIE* 4262, 414-419 (2001).
9. Denk, W., Strickler, J. H. & Webb, W. W. Two-photon laser scanning microscopy. *Science* 248, 73-76 (1990).